Journal of Materials Chemistry A

ROYAL SOCIETY OF CHEMISTRY

PAPER

View Article Online
View Journal | View Issue

Cite this: J. Mater. Chem. A, 2025, 13, 517

Light-induced degradation of methylammonium tin iodide absorber layers†

Joana Ferreira Machado, Jeremy Hieulle, Aline Vanderhaegen and Alex Redinger *

Light-induced degradation of tin-based organic inorganic halide perovskite (Sn-HOIP) absorbers is a major barrier for their deployment in photovoltaic applications. Sn-HOIPs are believed to intrinsically degrade due to the tendency of tin to change the oxidation state from (+2) to (+4). So far, most studies have been performed on absorbers that were synthesized with solvent-based techniques. The solvents themselves have been associated with Sn-HOIP degradation. Here, we show that in solvent-free coevaporated methylammonium tin iodide ($MASnI_3$) films exposed to white light, no Sn(+4) could be detected, even after almost 100 h of exposure. To understand the degradation mechanism, the chemical composition at the surface of $MASnI_3$ was measured by X-ray photoelectron spectroscopy after different illumination intervals. The measurements showed that $MASnI_3$ decomposed into tin iodide (SnI_2) and a minimal amount of metallic tin. The SnI_2 phase at the surface increases as a function of light exposure. Despite the strong degradation, light-induced decomposition was not accompanied by the formation of Sn(+4). In addition, the stability of SnI_2 under illumination was studied and compared to that of PbI_2. Here, SnI_2 did not show any degradation, in contrast to PbI_2, which degraded into metallic lead. Our results show that the tendency of tin to be in multiple oxidation states is not triggered by light. Instead, the critical point is the choice of an organic component (methylammonium) that leaves the perovskite crystal during illumination. These results show that it is essential to retain the organic component in the perovskite lattice, either by including additives or by replacing the organic component.

Received 6th September 2024
Accepted 3rd November 2024

DOI: 10.1039/d4ta06361a

rsc.li/materials-a

1 Introduction

Halide organic–inorganic perovskites are attracting attention in the photovoltaic community due to their fast evolution in power conversion efficiency (PCE). In little more than 10 years, the PCE of halide perovskites increased from 3.8% to 26.1% on the laboratory scale.[1–4] This record efficiency is comparable to the record for silicon solar cells, which is a well-established material for photovoltaic applications.[4,5]

Despite its extraordinary properties, the toxicity of lead remains one of the major challenges, as the residues of degraded lead perovskite can dissolve in water and this is a concern for public health and the environment.[6–8] So far, Sn-based perovskite solar cells have been considered the most promising replacement for Pb-based ones, with their PCE record already exceeding 14%.[9,10] This efficiency was obtained by doping a formamidinium tin iodide ($FASnI_3$) based absorber with tin fluoride (SnF_2), which has been reported to improve the stability and efficiency of Sn-based perovskites.[11–13]

Nevertheless, Sn-based solar cells are still less stable than their lead counterparts and their degradation has been attributed in numerous studies to the tendency of Sn to oxidize from Sn(+2) to Sn(+4) when exposed to moisture, oxygen, heat and light.[14,15] The degradation and low efficiencies are even more obvious in methylammonium tin iodide ($MASnI_3$) based solar cells, where the current record PCE is 7.13%.[16]

In terms of optoelectronic properties, $MASnI_3$ films exhibit high photoluminescence quantum yields and the peak has been reported to be around 1.3 eV, which corresponds to the optimum bandgap for single junction solar cells.[16–18] The same articles report very short carrier lifetimes, which were attributed to fast recombination due to defects and self-doping.

Multiple stability studies have been performed on Sn-based perovskites, where Sn-perovskites ($ASnX_3$) are found to easily oxidize and form double perovskites (A_2SnX_6)[19,20] or decompose into AI, SnO_2 and SnI_4 and eventually form I_2.[21] Note that A can be an organic cation, such as methylammonium or formamidinium, or an inorganic one, such as cesium. SnI_4 has been considered the main contributor to the degradation of Sn-perovskites and was even found to cause cyclic degradation of perovskite films.[15] Furthermore, Sn oxidation from the oxidation state of Sn(+2) to Sn(+4) has already been shown to cause self-p-doping in the absorber, resulting in loss of PCE.[15,22] This

Department of Physics and Materials Science, University of Luxembourg, Luxembourg City L-1511, Luxembourg. E-mail: alex.redinger@uni.lu

† Electronic supplementary information (ESI) available. See DOI: https://doi.org/10.1039/d4ta06361a

effect was found to be more predominant in $MASnI_3$ than in $FASnI_3$.[14]

It is worth mentioning that a large majority of the perovskite studies so far have been performed on absorbers that were synthesized *via* chemical, solvent-based methods. Although this growth method produces films for high-performance devices,[3,9] the use of dimethylsulfoxide (DMSO) as a solvent has also been associated with the oxidation of Sn in the precursor solution.[23–25] X-ray photoelectron measurements show that solvent-grown Sn-perovskite absorbers contain Sn(+4) even when they are fresh,[15,16,25–28] while thermally evaporated films with physical vapor deposition (PVD) can be grown without Sn(+4).[26,29]

From all the stresses that perovskites are sensitive to, light degradation seems to be of the highest importance, since every solar cell needs light to produce electricity. Therefore, it is not acceptable that light promotes the decomposition of solar cells and there is an urgent need to understand the exact mechanisms of degradation. Thorough studies of light degradation in perovskites have already been done. For lead perovskites, it was found that the degradation mechanism under light illumination is such that the Pb perovskite first degrades to PbI_2 and then PbI_2 degrades to Pb(0).[30–35]

Although there seems to be a consensus that MA^+ tends to leave the surface of methylammonium-containing perovskites upon illumination,[36–38] there is no clear agreement on the residues remaining on the surface of the sample.[28,38,39] Furthermore, all reports containing chemical analysis of Pb-free perovskites include only solvent-grown absorbers, adding another variable to their degradation study. A light degradation study of solvent-free Sn-perovskites is crucial for understanding light-induced degradation, without the deterioration effects of the solvents in the absorber.

In this study, we performed a detailed chemical analysis of light-degraded $MASnI_3$ absorbers that were grown using physical vapor deposition (PVD). This growth technique has previously been shown to form nominally Sn(+4)-free absorbers.[26] Additionally, the samples in this study were always kept in an inert gas or ultra-high vacuum (UHV) to minimize degradation due to contaminants such as oxygen or moisture. This is important since all external stresses are likely to contribute to degradation.

Compositional measurements were performed using X-ray photoelectron spectroscopy (XPS) after the sample was illuminated for different intervals of time. This technique is highly sensitive to changes in the composition and allowed us to distinguish between the different oxidation states of Sn, *i.e.* Sn(0), Sn(+2) and Sn(+4). The chemical analysis is complemented by surface measurement of topography and the work function of the fresh sample, using atomic force microscopy (AFM) and Kelvin probe microscopy (KPFM), which have been previously used to identify the presence of secondary phases, such as PbI_2, in Pb-perovskites.[31] Furthermore, photoluminescence (PL) and time-resolved photoluminescence (TRPL) measurements were performed to assess the quality of the fresh sample.

We show that $MASnI_3$ formed SnI_2 on the surface and lost MAI upon illumination. The degradation was not accompanied by the formation of Sn(+4), which highlights that the change in the oxidation state from +2 to +4 was not triggered by light. The KPFM measurements revealed no secondary phase on the $MASnI_3$ surface, unlike the observations typically made with Pb-containing perovskites. In contrast, our XPS results indicate that a uniform SnI_2 layer forms on the surface of the perovskite and thickens over time under illumination. From the temporal evolution of the elemental ratios, deduced by XPS, a model was developed that allowed us to estimate the thickness of the SnI_2 layer as a function of light exposure time.

Given the degradation mechanism and the tendency of Sn(+2) to decompose into Sn(+4),[15,22] complementary measurements of XPS were done on light exposed SnI_2 films. The impressive stability of SnI_2 under illumination indicated that the organic cation is the main cause of the degradation induced by the light of Sn perovskites. Interestingly, SnI_2 is much more stable against light exposure than PbI_2.

2 Methods

2.1 Synthesis

$MASnI_3$ samples were grown on ITO substrates using physical vapor deposition (PVD). Before deposition, ITO substrates, provided by Lumtec, were cut into approximately 7 mm squares, which were cleaned in a sequence of six ultrasonic baths at 50 °C. Each bath lasted 4 minutes and each contained a different liquid, namely an aqueous solution of Helmanex 2 wt%, DI water twice, ethanol, acetone, isopropanol and finally DI water. Then each substrate was blow dried with N_2 and ozone treated for 15 minutes. After the cleaning procedure, the substrates were immediately stored in a glovebox. The SnI_2 and the methylammonium iodide (MAI) powders were provided by Tokyo Chemical Industry (TCI), product number M2556. During thermal evaporation, the pressure was kept at 1×10^{-5} mbar with the source temperature of SnI_2 at $T = 265$ °C and the CH_3NH_3I powder was kept at a temperature between $T = 98$ °C and $T = 108$ °C such that the pressure in the chamber would be constant during deposition. The deposition time was set to 90 minutes to obtain films of approximately 300 nm thickness. The PVD was performed in a vacuum chamber embedded in a glovebox; therefore, the samples were never exposed to air or moisture and were always under a N_2 atmosphere or vacuum. The samples were transferred to the ultra-high vacuum (UHV) *via* dedicated suitcases.

The SnI_2 and the PbI_2 films were also deposited on ITO. The SnI_2 was evaporated at 265 °C, whereas the PbI_2 was evaporated at 300 °C. For every deposition, the substrate was at nominal room temperature $T = 21$ °C (±2 °C).

2.2 Characterization

XPS measurements were performed with a Prevac EA15 analyzer under UHV at a pressure of 5–9 $\times$ 10^{-10} mbar during the measurements. The X-ray source was a non-monochromatic Mg K_α source. During measurement, the acceleration voltage was

12 kV and the emission current was 25 mA. The pass energy was set to 50 eV and a rectangular lens slit of 2.5 cm × 25 mm was employed. The raw data from the $MASnI_3$ and SnI_2 samples were corrected for each element using Scofield factors and a calibration transmission function, which was determined by high resolution measurement of reference samples.[40]

In order to further reduce the systematic errors of the XPS system, PbI_2 and SnI_2 samples were used as standards to have the correct ratios for I/Sn and I/Pb. For each binding energy region, multiple individual high-resolution scans were performed to verify whether the sample exhibited charging. Since in this case there was no charging, the average of the scans was used.

The non-monochromatic X-ray source produces multiple emission lines, which produce satellite peaks in the measurement. In the case of Mg K_α, satellite peaks are expected with a shift of −8.4 eV and −10.2 eV in binding energy and a respective relative intensity of 8% and 4% compared to the main peak.[41] In the case of Sn3d and I3d orbitals, the satellite peak of the 3/2 peak overlaps with the main 5/2 peaks, and therefore satellite peaks have to be considered in the fitting.

The background signal was subtracted with W Tougaard and U2 Tougaard for Sn3d and I3d, respectively, and the Shirley background was used for C1s and N1s. The Sn3d and I3d peak fitting was performed with the Lorentzian asymmetric lineshapes LA and TLA, respectively, while the C1s and N1s were fitted with a Gaussian/Lorentzian sum (SGL) lineshape. Satellite peaks were fitted with Gaussian fitting.

Various fitting constraints were used for the XPS measurements. The energy separation between the spin–orbit split peaks 3/2 and 5/2 (ΔE_B) was fixed to 11.5 eV for the I3d peaks and 8.41 eV for Sn3d, according to the literature, for both the main peaks and the satellite peaks. Additionally, the 3/2 peak intensity was set to 2/3 of the 5/2 peak intensity and the full width at half maximum (FWHM) was the same for every peak of the same element. The FWHM of the Sn peaks and the binding energy of Sn(0) were determined by measuring and fitting a sputtered pure metallic tin plate. The binding energies of Sn(+2) and Sn(+4) were determined by measuring the same tin plate after oxidation (before sputtering under UHV) as described in ref. 26. Peak fitting was performed using CasaXPS software.

The sample was exposed to light in the XPS chamber, using a quartz tungsten-halogen lamp (Thorlabs QTH10) shining through a borosilicate vacuum viewport. The window was equipped with a lead-glass radiation protection (Allectra) to block X-ray radiation. Transmission measurements carried out on windows with and without the lead glass showed very little difference in the visible and near infrared light spectra. In order to avoid errors, the sample was never moved from its initial position for the whole set of measurements, with an irradiance of 16 $mW \cdot cm^{-2}$ (0.16 sun) at the sample position.

In order to assess the optoelectronic quality of the absorber layers, photoluminescence (PL) measurements are spectrally corrected and intensity calibrated to reproduce the illumination under 1 sun equivalent conditions according to the AM1.5 solar spectrum. The setup and calibration procedure are explained in ref. 42. Measurements were performed with an InGaAs detector (Andor iDus DU490A-1.7) ranging from 900 to 1600 nm. To excite the sample, a diode laser of wavelength 660 nm was used, with an output power of 2.61×10^{-1} W cm^{-2}, resulting in a corresponding photon flux of 2.17×10^{17} cm^2 s^{-1}.

Time-resolved photoluminescence (TRPL) measurement was performed using a pulsed laser with a wavelength of 639 nm. The duration of the laser pulse was approximately 70 ps and the excitation power density was estimated to be 4.584×10^{-2} W cm^{-2} at a repetition frequency of 20 MHz. During PL and TRPL measurements, the sample was placed in a box with a quartz window and constant N_2 flow.

Atomic force microscopy (AFM) and Kelvin probe force microscopy (KPFM) measurements were performed using an Omicron variable temperature scanning probe microscope (VT-SPM) in UHV operating in the low 10^{-10} mbar range. Topography measurements were performed in frequency modulation mode, with an excitation amplitude of 0.5 V at a frequency shift of −3 Hz. KPFM measurements were performed simultaneously with the topography measurements *via* side-band excitation in frequency modulation mode (FM mode), significantly increasing the measurement resolution by reducing the contribution from the large tip cone and from the cantilever. An AC voltage of 0.4 V was used at an oscillation frequency of 965 Hz. Additionally, for higher resolution, the tip used was the APEX high resolution tip, *i.e.* a doped diamond tip manufactured by Adama Innovations, with a quality factor (q-factor) in a vacuum of 9500 (±400).

3 Results and discussion

Before discussing the impact of light on $MASnI_3$, in-depth characterization of the PVD-grown films was carried out and is summarized in Fig. 1. Fig. 1(a) shows a typical topography of a $MASnI_3$ film measured by AFM under ultra-high vacuum directly after growth, where the typical polycrystalline structure of perovskites was visible.[43,44] Grains several hundred nanometers in size could be identified, separated by grain boundaries. In order to identify possible secondary phases, KPFM measurements were performed at the same spot. For the case of Pb-based halide perovskites, KPFM has proven to be extremely viable to identify secondary phases such as PbI_2, which exhibited distinct work functions compared to perovskites.[31] In fact, variations in the work function of approximately 300 meV were found as shown in Fig. 1(b) and in the work function distribution Fig. S1.† An average work function of 4.63 eV with a standard deviation of 0.05 eV was measured, which was in close agreement with the literature.[45]

Since the material was polycrystalline, differences in work function may arise as a result of not only different materials but also different crystallographic facets with distinct surface dipoles. A three-dimensional overlay of the topography and the work function shown in Fig. 1(c) suggests that most of the variations were due to different facets, since the low work function regions were restricted to parts of the grains only. From these measurements, we concluded that there were no obvious secondary phases at the surface of the films, which meant either that the film was phase pure or that the secondary

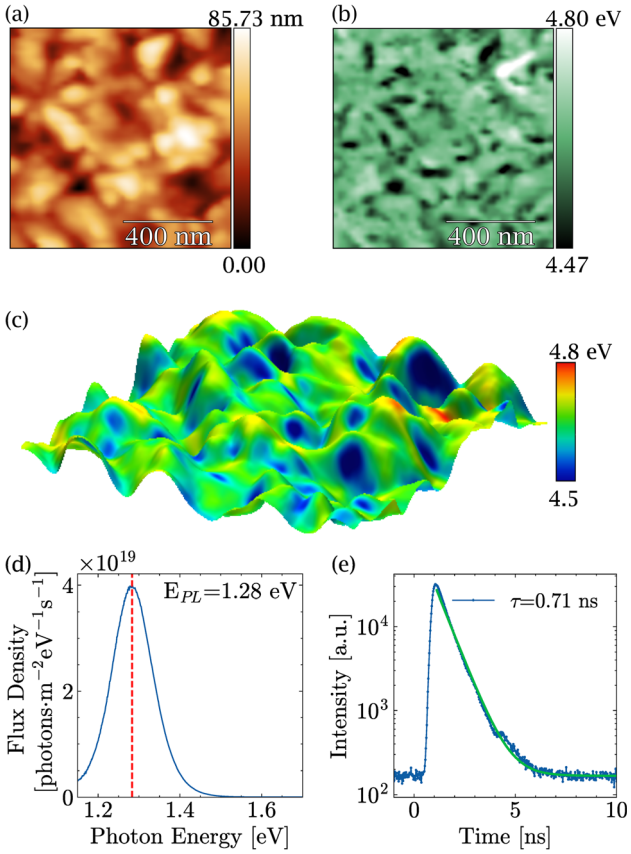

Fig. 1 Pristine $MASnI_3$: (a) AFM topography, (b) KPFM work function measured simultaneously with the topography, (c) 3D merging of the topography and the work function with color scale, (d) PL yield and (e) TRPL.

phase exhibited exactly the same work function as the perovskite.

The PL peak of $MASnI_3$ appeared at a value of 1.28 eV with a strong PL intensity (see Fig. 1(d)). From the calibrated measurements, a photoluminescence quantum yield $Q_e^{lum} = 2 \times 10^{-3}$. Q_e^{lum} was found to be in agreement with other samples synthesized *via* coevaporation.[26] The non-radiative losses, as estimated from $k_B T \times \ln(Q_e^{lum})$ amount to −155 meV, which is, *a priori*, a very favorable value for high-efficiency solar cells. The drawback of $MASnI_3$ is shown in Fig. 1(e), where TRPL measurements carried out on the pristine sample showed a decay time of only 0.71 ns, which is extremely fast compared to hundreds of nanoseconds of their lead counterparts.[46] Such PL intensity values and low lifetimes in $MASnI_3$ have been reported in multiple studies and have been attributed to fast carrier recombination and excessively doped absorbers,[16–18] which is in line with the results presented here.

The high Q_e^{lum} value combined with the fast decay time showed that these samples were highly doped. Using the formalism introduced in ref. 46, the doping level could be approximated to be 2×10^{18} cm^{-3}. The high doping levels in $MASnI_3$ have been justified by the presence of Sn(+4) in previous reports.[47]

Therefore, XPS was performed to measure the amount of Sn(+4) in the near surface region of the film. In order to identify the different oxidation states as precisely as possible, the coevaporated $MASnI_3$ films were always compared to reference SnI_2 films. Therefore, the position, FWHM and composition could be deduced with high accuracy. Fig. 2(a) shows a high resolution scan of the Sn3d region of a $MASnI_3$ film (top) and a SnI_2 film (bottom), where the Sn(+2) component is highlighted in yellow and the Sn(0) component is shown in red (see the Methods for the fitting procedure). Satellite peaks, due to the use of a non-monochromatic X-ray source, are shown in gray and had to be taken into account in the fitting of Sn3d, as they overlapped with the orbital Sn(+2). Fig. S2† highlights the difference in the Sn(0) fitting when the satellites are taken into account compared to when they are ignored.

The energy difference between the 3/2 orbital and the 5/2 orbital is denoted by ΔE_B. Note that within a single element, ΔE_B remained constant for the main peaks and for the satellite peaks. The positions of the satellite peaks for non-monochromatic sources are tabulated in ref. 41.

From the measurements shown in Fig. 2(a), it was found that the $MASnI_3$ films essentially contained Sn in the oxidation state (+2), as expected for pure $MASnI_3$ and in pristine SnI_2. There was probably a very small contribution of metallic Sn (oxidation state 0), although the quantity was very small and within the fit error, that is, 98% of Sn(+2) and 2% of Sn(0).

Note that Sn(0) was included in this fitting for consistency only. As shown later in the manuscript, the amount of Sn(0) increased as a result of light illumination. As a consequence, the Sn(0) component was already included in this spectrum. It should be stressed that, for the pristine sample shown here, the fitting result was equally fine without considering Sn(0). Importantly, the amount of Sn(+4) in the samples was lower than the detection limit. This was unexpected since the PL analysis and the high doping levels actually suggested that there was a considerable amount of Sn(+4).

The detailed scan in the I3d energy region is shown in Fig. 2(b). Similarly to the Sn region, the measurement was performed on $MASnI_3$ (top) and on SnI_2 (bottom). For both samples, the oxidation state I(−1) is shown in blue and the

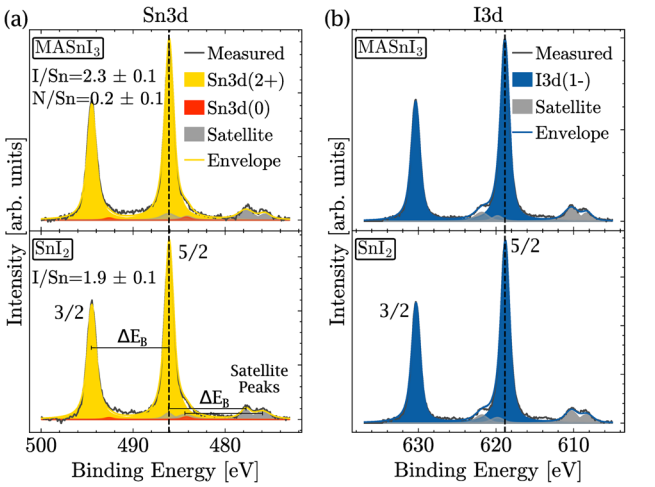

Fig. 2 Detailed XPS spectra of $MASnI_3$ (top) and SnI_2 (bottom) at (a) the Sn3d core-level and (b) the I3d core-level.

satellite peaks are shown in gray. Both samples only contained the oxidation state I(−1), which was the oxidation state expected for pure $MASnI_3$ and SnI_2 films.

Fig. 2(a) shows that the binding energies of Sn(+2) in $MASnI_3$ and SnI_2 were very similar (with only a 0.01 eV difference) and therefore it was not possible to identify an SnI_2 secondary phase in the $MASnI_3$ films by considering the binding energy only. The same conclusion held for the I3d binding energy in Fig. 2(b) (with a difference of 0.04 eV).

As discussed in the Methods section, the SnI_2 sample was used to calibrate the I/Sn ratio. For this particular sample, a value of 1.9 (±0.1) was deduced, which was expected. The I/Sn ratio deduced from the $MASnI_3$ sample equaled only 2.3 (±0.1) instead of the expected value of 3. Similarly, the measured N/Sn ratio was lower than the expected value, with 0.2 (±0.1) instead of 1. The only plausible secondary phase, which exhibited a ratio I/Sn that was lower than three combined with an oxidation state Sn(+2), was SnI_2.

Therefore, we speculated that the discrepancy in the ratio for $MASnI_3$ was probably caused by a thin layer of SnI_2 on top of the perovskite. The presence of $MASnI_3$ and SnI_2 was also confirmed by X-ray diffraction (Fig. S3†), where reflection peaks are visible for both materials. Furthermore, since XPS provides the chemical composition of the topmost 10 nm, the low I/Sn and low N/Sn ratios do not contradict the bulk-sensitive PL and XRD measurements, which showed that the 300 nm thick sample is indeed MASI perovskite. XPS provides further information on the chemical composition of the top surface of the sample. To identify the source of this deviation, light-induced degradation of $MASnI_3$ was investigated. In order to gain a full picture of the compositional changes occurring at the surface, tin, iodine, carbon, nitrogen, and oxygen signals were monitored as a function of white light exposure time.

The light-induced degradation measurements were made in the following way: a pristine $MASnI_3$ sample was exposed to light in a vacuum for different time intervals. After each interval, it was measured using XPS. All variations in composition that could be due to XPS or vacuum degradation were taken into account in the measurement error bar. The total exposure time to light summed up to 61 hours. Fig. 3(a) shows the spectra in the Sn3d energy region performed on a pristine sample and after 61 h of light exposure. For better visibility, the Sn(+2) peaks and the satellite peaks were omitted, but were taken into account in the fit. A small increase in Sn(0) was observed, but no formation of Sn(+4) was detected. Fig. 3(b) shows the background subtracted raw data in the Sn3d 3/2 peak region. A small shoulder formed on the lower binding energy side, which was due to the higher content of Sn(0). Note that in the Sn3d 3/2 peak, there was no contribution from the satellite peaks, which makes the identification of Sn(0) much easier. We would like to stress that the changes observed for Sn(0) were small and usually such variations are difficult to interpret. In the present case, the position of the sample did not change at all and all measurements were done consecutively, which was the only way to measure such small differences.

Note that the topography of the sample does not change significantly after light exposure (see Fig. S4†), making it impossible to identify the degradation through topography.

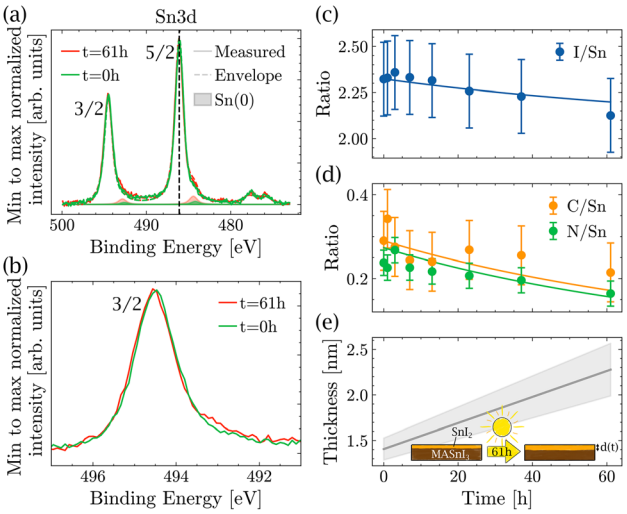

Fig. 3 Degradation of $MASnI_3$ with light over 61 h. (a) XPS measurements of the pristine sample (green) and the sample after 61 h of illumination (red) with envelope and Sn(0), and (b) zoomed-in view of the Sn 3d 3/2 peak, showing only raw data with the background subtracted. (c) Evolution of the I/Sn (c), C/Sn and N/Sn (d) ratios with the illumination time of the sample and fitting using a bi-layer model. (e) Estimation of the thickness of SnI_2 over time.

Furthermore, as mentioned previously, it was not possible to track the degradation by looking at the binding energy of the peaks alone. The peak position of Sn(3d) did not change during light exposure. However, when looking at the ratios of I/Sn, C/Sn and N/Sn (Fig. 3(c) and (d)), all three ratios decreased as a function of light exposure, suggesting that the amount of MAI decreased as a function of time.

In the literature, $MAPbI_3$ is known to degrade into MAI (or fragments of MAI) and PbI_2.[31,33,34] Assuming that $MASnI_3$ has a degradation pathway similar to that of $MAPbI_3$, then MAI losses increase the amount of SnI_2 in the films and the reaction is as described by eqn (1).

$$MASnI_3(s) \xrightarrow{h\nu} MAI(g) + SnI_2(s) \quad (1)$$

That is, if MAI is assumed to leave the $MASnI_3$ surface in gas form, then the ratio I/Sn goes from 3 to 2 and the ratio N/Sn goes from 1 to 0. Here, MAI is considered as the entire MAI molecule, but it could also be smaller fragments of MAI.

To test whether the degradation pathway proposed in eqn (1) is valid and compatible with the measured XPS ratios, a two-layer model was used, which is described below. Since the I/Sn ratio was lower than 3 already at the beginning of the measurement, it is plausible to assume that a thin layer of SnI_2 was already present from the beginning. If $MASnI_3$ decomposes according to eqn (1), then the thickness of SnI_2 should increase over time. Consequently, changes in elemental ratios should allow one to deduce the increase in the thickness of the SnI_2 layer as a function of time.

This two-layer model is well established in the XPS community and, for instance, described in the book by Hofmann and Siegfried.[41] The measured intensity of an element x

in a two-layer system has two contributions: one related to the surface material and the other related to the bulk material. The surface contribution increases exponentially with the thickness d of the top layer, whereas the bulk contribution decreases exponentially with d. The intensity of an element x can therefore be expressed as

$$I_x = I_{x,surf}\left[1 - \exp\left(\frac{-d}{\lambda_x \cos\theta}\right)\right] + I_{x,bulk}\exp\left(\frac{-d}{\lambda_x \cos\theta}\right). \quad (2)$$

I_x is the measured intensity divided by the sensitivity factors determined by Scofield,[40] and $I_{x,surf}$ and $I_{x,bulk}$ are the intensities of the element x in the pure surface material and in the pure bulk material, respectively. θ is the angle between the normal of the sample surface and the analyzer lenses, in the framework of this study $\theta = 0°$, and λ_x is the inelastic mean free path (IMFP) of the element x in the surface material. It is worth mentioning that in the formula established by Hofmann and Siegfried, λ_x stands for the effective attenuation length (EAL) of the electrons of the element x in the surface materials. The EAL depends on both the elastic and inelastic scattering, but here, for simplicity, the elastic scattering contribution is neglected and the inelastic mean free path (IMFP) is used instead. According to Hofmann and Siegfried, this approximation introduces an error of 10–15% in the value of λ.

Here, the value of interest was the ratio between x and Sn (x/Sn or $R_{x,Sn}$ for better readability), which can be obtained by dividing the intensity I_x by I_{Sn}. The complete derivation of this ratio can be found in the ESI (Section 4),† and the final equation for this ratio is given by

$$R_{x,Sn} = \frac{R_{surf} \times \rho_{Sn}\left(1 - e^{-d/\lambda_x}\right) + R_{bulk} \times e^{-d/\lambda_x}}{\rho_{Sn}\left(1 - e^{-d/\lambda_{Sn}}\right) + e^{-d/\lambda_{Sn}}}. \quad (3)$$

R_{surf} and R_{bulk} are the expected ratios x/Sn in the surface layer and in the bulk, respectively, and ρ_{Sn} is the ratio of the volume density of Sn in the bulk and on the surface.

Assuming that the SnI_2 formation occurs layer by layer, then the thickness d was a function of the light exposure time t. Furthermore, the initial thickness of the $MASnI_3$ layer (approximately 300 nm) was two orders of magnitude larger than the SnI_2 thickness; therefore, it was considered as an infinite reservoir. As a consequence, degradation evolved linearly in time and therefore $d(t) = d(0) + b \times t$, where $d(0)$ is the initial thickness of the SnI_2 layer and b is the $MASnI_3$ decomposition rate under light exposure.[48]

The datasets of N/Sn, C/Sn and I/Sn were fitted with $d(0)$, b and ρ_{Sn} as free parameters, such that they are the same for all three data sets. The IMFPs were calculated using the model derived by Tanuma *et al.* (TPP2M).[49] From the fitting, an initial SnI_2 thickness $d(0)$ of 1.4 ± 0.1 nm was obtained and the thickness $d(t)$ increased at a rate of $b = 0.014 \pm 0.003$ nm h^{-1}. The ratio of Sn in the overlayer to the bulk was $\rho_{Sn} = 2.71 \pm 0.33$, which was in good agreement with the tabulated values $\rho_{Sn}^{calc} = 4.2$ (see Section 5 of the ESI†). According to the model, after 61 h of exposure to light, the SnI_2 reaches a thickness of $d(61\text{ h}) = 2.3 \pm 0.3$ nm, representing an almost two-fold increase.

The KPFM-measured work functions also confirmed this model. In fact, the work function of $MASnI_3$ decreases from 4.63 eV in the pristine sample to 4.61 eV after illumination, which is a negligible variation. This work function was very similar to the work function of SnI_2 (4.7 eV), which was confirmed on an SnI_2 only sample.

The degradation of $MASnI_3$ in SnI_2 was similar to what was observed in previous reports for Pb-based perovskites,[30–35] which degrade into PbI_2. However, the same reports mention that PbI_2 additionally decomposed into Pb(0). Surprisingly enough, in the data shown here only a minimal amount of Sn(0) was observed and the Sn(+4) remained lower than the detection limit for the duration of the experiment. To assess the stability of SnI_2 against light, a degradation study was performed on films of pure SnI_2 and pure PbI_2. This allowed for a comparison of their degradation upon exposure to light.

Fig. 4(a) shows the ratio I/Sn of SnI_2 and the ratio I/Pb of PbI_2 as a function of illumination time. Although both ratios were similar at time $t = 0$ h, the I/Sn ratio in SnI_2 remained stable for almost 100 h of light exposure, while the I/Pb ratio in PbI_2 started to decrease after 4 h of exposure and continued to decrease over time. Similarly, in Fig. 4(b), the Sn(0) content in SnI_2 was negligible and remained stable under long-duration illumination, while the Pb(0) content increased significantly over time. No Sn(+4) formation was observed upon illumination of SnI_2. This set of measurements showed that SnI_2 was much more stable than PbI_2 under illumination in UHV and the secondary phases of SnI_2 in $MASnI_3$ will not degrade further into Sn(0), unlike Pb-based perovskites.

Finally, Fig. 5 shows the evolution of Sn(0) in $MASnI_3$ and SnI_2 under illumination. Notice that while the quantity of Sn(0) increased when $MASnI_3$ was illuminated, the quantity of Sn(0) in SnI_2 remained stable. This is an important result, as the formation of metallic Sn in $MASnI_3$ was not triggered by the decomposition of SnI_2 but by the perovskite itself. Recalling eqn (1), the light-induced degradation pathway must be written as

$$MASnI_3(s) \xrightarrow{h\nu} MAI(g) + A \times SnI_2(s) + (1 - A) \times [Sn(s) + I_2(g)] \quad (4)$$

The factor A is a value between zero and unity and describes the probability that MASI decomposes into SnI_2 *versus* a direct decomposition into metallic Sn. In Pb-based perovskites, the direct decomposition of $MAPbI_3$ into metallic Pb was very

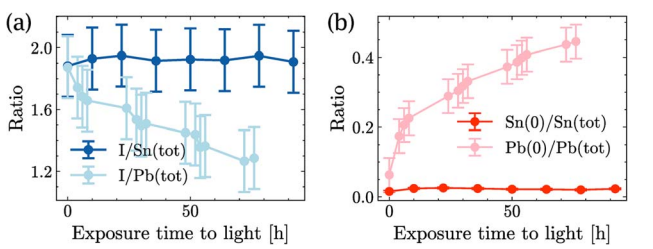

Fig. 4 Time evolution of SnI_2 and PbI_2 under light illumination: (a) quantity of iodide and (b) quantity of Sn(0) in SnI_2 and quantity of Pb(0) in PbI_2.

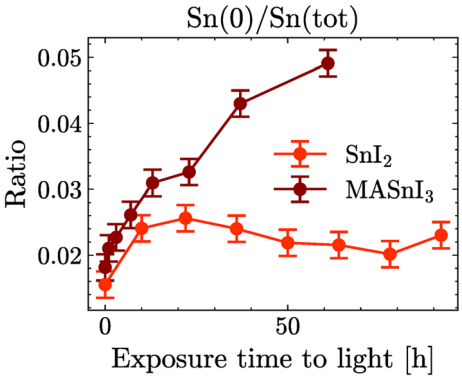

Fig. 5 Evolution of Sn(0) in $MASnI_3$ and in SnI_2 with light exposure.

difficult to measure *via* XPS since it was shown that PbI_2 decomposed into metallic Pb at a faster rate than Pb-based perovskites.[31] However, for Sn-based perovskites, this could now be measured directly, as SnI_2 does not seem to be photosensitive.

The constant value of Sn(0) in SnI_2 should also be discussed. The value was extremely small, but still outside the statistical error of the fit. However, this did not mean that the Sn(0) value was in fact greater than zero in the SnI_2 films. The background in XPS and the lineshape also impacted the fit result. Our current understanding is that the Sn(0) in SnI_2 is likely to be the resolution limit. Importantly, the increase of the Sn(0) in $MASnI_3$ is not impacted by this since pristine samples showed very similar values for Sn(0) to those in SnI_2, which then increased, while keeping the fit routine constant.

Most importantly, the light instability of $MASnI_3$ under vacuum is not due to a change in the oxidation state from Sn(+2) to Sn(+4). Therefore, light-induced degradation is not triggered by the instability of the oxidation state of Sn. In fact, here Sn is shown to be even more tolerant than Pb. Instead, the light-induced decomposition of $MASnI_3$ appears to arise from the choice of the organic component. As calculations in the literature have shown, MA^+ in the perovskite lattice has strong dynamics.[50–52] The organic cation moves and rotates with the cage, causing lattice distortion and lattice softness. This motion is probably reinforced by light exposure, where additional energy is given to the system, which contributes to the instability of $MASnI_3$. This also means that the best way to stabilize Sn-based perovskites is to move away from MAI, which is the source of intrinsic instability in the perovskite. Importantly, the SnI_2 secondary phase is not photosensitive, which offers a great advantage compared to the Pb-based system. In the state-of-the-art Pb-based perovskite, residual PbI_2 will lead to long-term stability problems, which can be prevented by the use of Sn.

3.1 Summary

In this study, we used XPS, KPFM and photoluminescence based techniques to understand light-induced degradation of $MASnI_3$. In contrast to most reports in the literature, we show that, in UHV, decomposition of the near surface region does not induce Sn(+4). Most of the $MASnI_3$ transforms into SnI_2 when exposed to light and a negligible amount into Sn(0). In contrast to Pb-based halide perovskites, SnI_2 does not decompose into Sn(0) and I_2 but remains stable against prolonged light exposure. This is certainly a big advantage for Sn-based perovskites compared to Pb-based ones. Despite the improved stability of SnI_2 compared to PbI_2, high doping levels are also problematic for coevaporated Sn-based perovskites. Despite the fact that we did not detect any Sn(+4), the combination of PLQY and TRPL allowed us to deduce doping levels in the order of 10^{18} cm^{-3}. In order to make Sn-based perovskites a true alternative to Pb-containing ones, the use of MAI needs to be prevented and the doping level needs to be reduced to an acceptable level. Our research suggests that the high doping levels in Sn-based perovskites are not due to the presence of Sn(+4), as previously thought in the literature. To advance the development of lead-free perovskite solar cells, it is crucial to identify the real source of this high doping in Sn-based perovskites. This knowledge will enable the formulation of effective strategies to control doping levels in these materials.

Furthermore, we have found that the photochemical conversion of $MASnI_3$ into SnI_2 is a major factor limiting the long-term intrinsic stability of Sn-based perovskites. A more detailed investigation into the photochemical stability of Sn-based perovskites is necessary to propose mitigation strategies, such as the use of different organic cations or encapsulation methods.

Data availability

The data supporting this article have been included as part of the article and the ESI.† Raw data files can be sent to the reader upon reasonable request.

Conflicts of interest

There are no conflicts to declare.

Acknowledgements

The authors acknowledge funding from the Deutsche Forschungsgemeinschaft (DFG, German Research Foundation) within SPP 2196 (project number 423876021) and the Luxembourg National Research Fund (FNR) (grant references: 11244141, 13390539, and 14757355). The authors acknowledge Anastasios-Sevastianos Antoniou for measuring the SnI_2 work function. Susanne Siebentritt and Ricardo Poeira for useful discussions. The authors acknowledge technical support of B. Uder, U. Siegel, and R. Himelrick.

References

1 A. Kojima, K. Teshima, Y. Shirai and T. Miyasaka, *J. Am. Chem. Soc.*, 2009, **131**, 6050–6051.
2 University of Science and Technology of China (USTC), *USTC Set New Record in Perovskite Cell Efficiency*, 2023, **https://en.ustc.edu.cn/info/1007/4676.htm**, accessed: 2024-06-01.

3 Z. Liang, Y. Zhang, H. Xu, W. Chen, B. Liu, J. Zhang, H. Zhang, Z. Wang, D. H. Kang, J. Zeng, X. Gao, Q. Wang, H. Hu, H. Zhou, X. Cai, X. Tian, P. Reiss, B. Xu, T. Kirchartz, Z. Xiao, S. Dai, N. G. Park, J. Ye and X. Pan, *Nature*, 2023, **624**, 557–563.
4 National Renewable Energy Laboratory (NREL), *Best Research-Cell Efficiency Chart*, 2024, **https://www.nrel.gov/pv/cell-efficiency.html**, accessed: 2024-05-28.
5 LONGi, *LONGi Sets a New World Record of 27.09% for the Efficiency of Silicon Heterojunction Back-Contact (HBC) Solar Cells*, 2023, **https://www.longi.com/en/news/heterojunction-back-contact-battery/**, accessed: 2024-06-01.
6 J. Li, H. L. Cao, W. B. Jiao, Q. Wang, M. Wei, I. Cantone, J. Lü and A. Abate, *Nat. Commun.*, 2020, **11**, 1–5.
7 A. Babayigit, D. Duy Thanh, A. Ethirajan, J. Manca, M. Muller, H. G. Boyen and B. Conings, *Sci. Rep.*, 2016, **6**, 1–11.
8 A. Babayigit, A. Ethirajan, M. Muller and B. Conings, *Nat. Mater.*, 2016, **15**, 247–251.
9 B. B. Yu, Z. Chen, Y. Zhu, Y. Wang, B. Han, G. Chen, X. Zhang, Z. Du and Z. He, *Adv. Mater.*, 2021, **33**, 1–10.
10 G. Liu, X. Jiang, W. Feng, G. Yang, X. Chen, Z. Ning and W. Q. Wu, *Angew. Chem., Int. Ed.*, 2023, **62**, 1–10.
11 M. H. Kumar, S. Dharani, W. L. Leong, P. P. Boix, R. R. Prabhakar, T. Baikie, C. Shi, H. Ding, R. Ramesh, M. Asta, M. Graetzel, S. G. Mhaisalkar and N. Mathews, *Adv. Mater.*, 2014, **26**, 7122–7127.
12 T. M. Koh, T. Krishnamoorthy, N. Yantara, C. Shi, W. L. Leong, P. P. Boix, A. C. Grimsdale, S. G. Mhaisalkar and N. Mathews, *J. Mater. Chem. A*, 2015, **3**, 14996–15000.
13 A. G. Kontos, A. Kaltzoglou, E. Siranidi, D. Palles, G. K. Angeli, M. K. Arfanis, V. Psycharis, Y. S. Raptis, E. I. Kamitsos, P. N. Trikalitis, C. C. Stoumpos, M. G. Kanatzidis and P. Falaras, *Inorg. Chem.*, 2017, **56**, 84–91.
14 F. Wang, J. Ma, F. Xie, L. Li, J. Chen, J. Fan and N. Zhao, *Adv. Funct. Mater.*, 2016, **26**, 3417–3423.
15 L. Lanzetta, T. Webb, N. Zibouche, X. Liang, D. Ding, G. Min, R. J. E. Westbrook, B. Gaggio, T. J. Macdonald, M. S. Islam and S. A. Haque, *Nat. Commun.*, 2021, **12**, 2853.
16 F. Li, C. Zhang, J. H. Huang, H. Fan, H. Wang, P. Wang, C. Zhan, C. M. Liu, X. Li, L. M. Yang, Y. Song and K. J. Jiang, *Angew. Chem., Int. Ed.*, 2019, **58**, 6688–6692.
17 N. K. Noel, S. D. Stranks, A. Abate, C. Wehrenfennig, S. Guarnera, A. A. Haghighirad, A. Sadhanala, G. E. Eperon, S. K. Pathak, M. B. Johnston, A. Petrozza, L. M. Herz and H. J. Snaith, *Energy Environ. Sci.*, 2014, **7**, 3061–3068.
18 W. Ke, C. C. Stoumpos, I. Spanopoulos, L. Mao, M. Chen, M. R. Wasielewski and M. G. Kanatzidis, *J. Am. Chem. Soc.*, 2017, **139**, 14800–14806.
19 D. J. Kubicki, D. Prochowicz, E. Salager, A. Rakhmatullin, C. P. Grey, L. Emsley and S. D. Stranks, *J. Am. Chem. Soc.*, 2020, **142**, 7813–7826.
20 X. Qiu, B. Cao, S. Yuan, X. Chen, Z. Qiu, Y. Jiang, Q. Ye, H. Wang, H. Zeng, J. Liu and M. G. Kanatzidis, *Sol. Energy Mater. Sol. Cells*, 2017, **159**, 227–234.
21 T. Leijtens, R. Prasanna, A. Gold-Parker, M. F. Toney and M. D. McGehee, *ACS Energy Lett.*, 2017, **2**, 2159–2165.
22 D. Ricciarelli, D. Meggiolaro, F. Ambrosio and F. De Angelis, *ACS Energy Lett.*, 2020, **5**, 2787–2795.
23 M. I. Saidaminov, I. Spanopoulos, J. Abed, W. Ke, J. Wicks, M. G. Kanatzidis and E. H. Sargent, *ACS Energy Lett.*, 2020, **5**, 1153–1155.
24 J. Pascual, D. Di Girolamo, M. A. Flatken, M. H. Aldamasy, G. Li, M. Li and A. Abate, *Chem.–Eur. J.*, 2022, **28**, 1–7.
25 C. Ge, B. Jiang, J. Zhu, P. Zhang, R. Ma, S. Yan, Z. Liu, A. Shaker, M. S. Salem, J. Luo, L. Xu, J. K. Yang, Z. Li, H. Song, C. Chen and J. Tang, *Adv. Funct. Mater.*, 2024, **2400075**, 1–8.
26 A. Singh, J. Hieulle, J. F. Machado, S. Gharabeiki, W. Zuo, M. U. Farooq, H. Phirke, M. Saliba and A. Redinger, *Nano Lett.*, 2022, **22**, 7112–7118.
27 Z. Dai, T. Lv, J. Barbaud, W. Tang, T. Wang, L. Qiao, H. Chen, R. Zheng, X. Yang and L. Han, *Sci. China Mater.*, 2021, **64**, 2645–2654.
28 X. Liu, Y. Wang, T. Wu, X. He, X. Meng, J. Barbaud, H. Chen, H. Segawa, X. Yang and L. Han, *Nat. Commun.*, 2020, **11**, 1–7.
29 M. Abbasli, J. Hieulle, J. Schrage, D. Wilks, A. Samad, U. Schwingenschlögl, A. Redinger, C. Busse and R. Ohmann, *Adv. Funct. Mater.*, 2024, **34**(40), 2403680.
30 N. H. Nickel, F. Lang, V. V. Brus, O. Shargaieva and J. Rappich, *Adv. Electron. Mater.*, 2017, **3**, 1–9.
31 J. Hieulle, A. Krishna, A. Boziki, J. N. Audinot, M. U. Farooq, J. Ferreira Machado, M. Mladenović, H. Phirke, A. Singh, T. Wirtz, A. Tkatchenko, M. Graetzel, A. Hagfeldt and A. Redinger, *Energy Environ. Sci.*, 2024, **17**, 284–295.
32 J. Yang, Q. Hong, Z. Yuan, R. Xu, X. Guo, S. Xiong, X. Liu, S. Braun, Y. Li, J. Tang, C. Duan, M. Fahlman and Q. Bao, *Adv. Opt. Mater.*, 2018, **6**, 1–8.
33 X. Tang, M. Brandl, B. May, I. Levchuk, Y. Hou, M. Richter, H. Chen, S. Chen, S. Kahmann, A. Osvet, F. Maier, H. P. Steinrück, R. Hock, G. J. Matt and C. J. Brabec, *J. Mater. Chem. A*, 2016, **4**, 15896–15903.
34 W. C. Lin, W. C. Lo, J. X. Li, Y. K. Wang, J. F. Tang and Z. Y. Fong, *npj Mater. Degrad.*, 2021, **5**, 1–6.
35 S. Svanström, A. García Fernández, T. Sloboda, T. J. Jacobsson, H. Rensmo and U. B. Cappel, *Phys. Chem. Chem. Phys.*, 2021, **23**, 12479–12489.
36 L. Huerta Hernandez, M. A. Haque, A. Sharma, L. Lanzetta, J. Bertrandie, A. Yazmaciyan, J. Troughton and D. Baran, *Sustainable Energy Fuels*, 2022, **6**, 4605–4613.
37 C. Li, Z. Song, C. Chen, C. Xiao, B. Subedi, S. P. Harvey, N. Shrestha, K. K. Subedi, L. Chen, D. Liu, Y. Li, Y. W. Kim, C. s. Jiang, M. J. Heben, D. Zhao, R. J. Ellingson, N. J. Podraza, M. Al-Jassim and Y. Yan, *Nat. Energy*, 2020, **5**, 768–776.
38 A. F. Akbulatov, S. A. Tsarev, M. Elshobaki, S. Y. Luchkin, I. S. Zhidkov, E. Z. Kurmaev, S. M. Aldoshin, K. J. Stevenson and P. A. Troshin, *J. Phys. Chem. C*, 2019, **123**, 26862–26869.
39 J. Sanchez-Diaz, R. S. Sánchez, S. Masi, M. Krecmarová, A. O. Alvarez, E. M. Barea, J. Rodriguez-Romero,

V. S. Chirvony, J. F. Sánchez-Royo, J. P. Martinez-Pastor and I. Mora-Seró, *Joule*, 2022, **6**, 861–883.
40 J. H. Scofield, *J. Electron Spectrosc. Relat. Phenom.*, 1976, **8**, 129–137.
41 S. Hofmann, *Auger- and X-Ray Photoelectron Spectroscopy in Materials Science: A User-Oriented Guide*, 2013.
42 A. J. M. Prot, M. Melchiorre, F. Dingwell, A. Zelenina, H. Elanzeery, A. Lomuscio, T. Dalibor, M. Guc, R. Fonoll-Rubio, V. Izquierdo-Roca, G. Kusch, R. A. Oliver and S. Siebentritt, *APL Mater.*, 2023, **11**, 1–11.
43 T. Gallet, R. G. Poeira, E. M. Lanzoni, T. Abzieher, U. W. Paetzold and A. Redinger, *ACS Appl. Mater. Interfaces*, 2021, **13**, 2642–2653.
44 E. M. Lanzoni, T. Gallet, C. Spindler, O. Ramírez, C. K. Boumenou, S. Siebentritt and A. Redinger, *Nano Energy*, 2021, **88**, 106270.
45 T. Hellmann, M. Wussler, C. Das, R. Dachauer, I. El-Helalya, C. Mortan, T. Mayer and W. Jaegermann and We, *J. Mater. Chem. C*, 2019, **7**, 5324–5332.
46 T. Kirchartz, J. A. Márquez, M. Stolterfoht and T. Unold, *Adv. Energy Mater.*, 2020, **1904134**, 1–21.
47 Y. Takahashi, H. Hasegawa, Y. Takahashi and T. Inabe, *J. Solid State Chem.*, 2013, **205**, 39–43.
48 R. H. Petrucci, F. G. Herring, J. D. Madura and C. Bissonnette, *General Chemistry: Principles and Modern Applications*, 2017.
49 S. Tanuma, C. J. Powell and D. R. Pen, *Surf. Interface Anal.*, 1994, **21**, 165–176.
50 R. Wasylishen, O. Knop and J. B. Macdonald, *Solid State Commun.*, 1985, **56**, 581–582.
51 A. M. Leguy, J. M. Frost, A. P. McMahon, V. G. Sakai, W. Kochelmann, C. Law, X. Li, F. Foglia, A. Walsh, B. C. O'Regan, J. Nelson, J. T. Cabral and P. R. Barnes, *Nat. Commun.*, 2015, **6**, 1–3.
52 K. Fykouras, J. Lahnsteiner, N. Leupold, P. Tinnemans, R. Moos, F. Panzer, G. A. de Wijs, M. Bokdam, H. Grüninger and A. P. Kentgens, *J. Mater. Chem. A*, 2023, **11**, 4587–4597.